Automatic Monitor-Based Tuning of an RF Silicon Photonic 1X4 Asymmetric Binary Tree True-Time-Delay Beamforming Network

Gihoon Choo, *Student Member, IEEE*, Christi K. Madsen, *Senior Member, IEEE, Fellow, OSA*, Samuel Palermo, *Senior Member, IEEE*, and Kamran Entesari, *Senior Member, IEEE*

***Abstract*—Photonic beamforming networks are promising candidates to achieve power-efficient transmission in future cellular communication systems. However, sensitivity to process and temperature variations necessitates an automatic calibration solution to enable robust operation. This paper demonstrates fully automatic monitor-based tuning of an integrated optical ring resonator-based 1X4 asymmetric binary tree optical beamforming network (OBFN). The proposed monitor-based tuning algorithm compensates fabrication variations and thermal crosstalk by controlling micro-heaters individually using information from electrical monitors. This algorithm is demonstrated on an OBFN that operates at 30 GHz with 2 GHz bandwidth and is fabricated in a standard silicon photonics foundry process. Successful calibration of the OBFN from a severely degraded initial response to the well-defined group delay responses required for a targeted radiating angle over 60° (−30° to 30°) in a linear beamforming antenna array is achieved. This fully automatic tuning approach opens the possibility of employing silicon OBFNs in real wideband mm-wave wireless communication systems.**

***Index Terms*—Microwave photonics, optical beamforming, optical ring resonators, phased arrays, photonic integrated circuits, RF photonics, thermal crosstalk, true time delays.**

I. Introduction

CONTINUOUS growth in wireless data traffic makes millimeter wave (mm-wave) frequencies more attractive due to abundantly available spectrum, compact antenna size, and potential use in commercial 5G applications [1], [2]. An important part of a mm-wave 5G cellular communications transceiver is an antenna array that allows for power-efficient transmission, avoidance of overlap between communication cells, and modification of the coverage range of a single base station [3]. Within the antenna array system, the beamforming network plays a critical role by providing beam focusing and steering to a specific direction. Unfortunately, conventional electronic beamforming networks that operate in the mm-wave range face significant challenges in achieving the required instantaneous bandwidth and high beam steering resolution in a small form factor. Integrated microwave photonic circuits offer a potential solution due to their broadband operation, immunity to electromagnetic interference, and compact size.

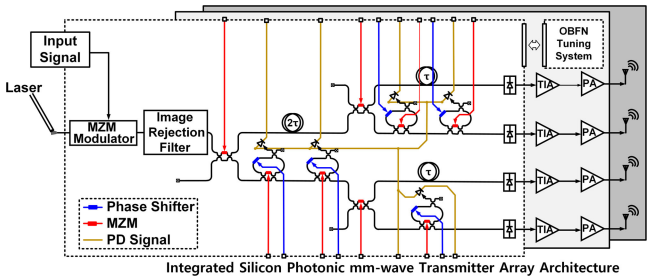

Fig. 1. Conceptual integrated silicon photonic ORR-based mm-wave beamforming transmitter array.

Conventional electronic beamforming systems based on phase shifters display frequency-dependent behavior, called beam squint [4], [5]. Thus, antenna array systems require true time-delay (TTD) beamforming to obtain wide instantaneous bandwidth and squint-free operation of the antenna array [6]–[8]. Several photonic approaches have been proposed to address this. An intuitive approach involves using a TTD network consisting of fixed-length optical fibers and sets of switchable fiber delay lines to create discrete delay differences [9]. Other fiber-based solutions include utilizing either a fiber optic prism [10] or fiber Bragg-gratings [11]–[13] to create variable delays for different source wavelengths. While these fiber-based systems perform well, they are relatively bulky. Integrated photonic beamforming networks offer a dramatic reduction in form factor. One integrated approach utilizes a TTD network with integrated waveguide delay lines and switch elements to provide discrete delay differences [14]–[16]. This allows for simple switching control, but the discrete delays limit the beam scanning resolution. Another approach utilizes optical ring resonators (ORRs) as tunable delay elements, with a conceptual integrated silicon photonic mm-wave beamforming transmitter array that employs an ORR-based beamforming network shown in Fig. 1. ORR-based beamforming networks have been successfully demonstrated with different platforms [17]–[22], and combinations of ORRs and switchable delay lines have also been shown to realize large delays with continuous tuning capability [23].

Manuscript received July 18, 2018; revised September 13, 2018; accepted September 14, 2018. Date of publication October 1, 2018; date of current version October 25, 2018. This work was supported by the National Science Foundation through Award 1807281. *(Corresponding author: Gihoon Choo.)*

The authors are with the Department of Electrical and Computer Engineering, Texas A&M University, College Station, TX 77843 USA (e-mail: jujjh0127@tamu.edu; cmadsen@tamu.edu; spalermo@tamu.edu; kentesar@tamu.edu).

Color versions of one or more of the figures in this paper are available online at http://ieeexplore.ieee.org.

Digital Object Identifier 10.1109/JLT.2018.2873199

While ORR-based beamforming has the potential to allow for continuous tuning, this necessitates precise control of the ORRs. A major drawback of reported ORR-based beamforming networks is the difficulty of calibrating the original response in the presence of fabrication and temperature variations. Integrated heaters are most commonly utilized for tuning these structures via the thermo-optic effect. Current demonstrations are manually tuned and rely on output monitoring, which is time consuming and costly. Thermal crosstalk between phase shifters in the integrated photonic chips exasperate this process, often requiring simultaneous monitoring of each output with multiple optical vector network analyzers (OVNAs).

This paper presents a fully automatic monitor-based tuning algorithm for a 1X4 silicon photonic ORR-based asymmetric binary tree OBFN. Added drop ports and photodetectors in each ORR provide electrical information to automatically tune all OBFN outputs simultaneously. To the best of our knowledge, this is the first demonstration of automatic OBFN tuning with an integrated electrical monitoring approach. Building upon the scheme described in [24], this work demonstrates multiple successful calibrated results that correspond to different beam directions in a beamforming antenna array. Section II details the design of the ORR-based beamforming network that operates at 30 GHz with 2 GHz bandwidth and also introduces the automatic monitor-based tuning algorithm. Photonic device design and fabrication details are discussed in Section III. Section IV presents experimental calibration of the 1X4 silicon photonic ORR-based beamforming network and discusses the corresponding beam pattern of the antenna array. A discussion of thermal crosstalk, design optimization, and comparison with other silicon photonic beamforming networks is provided in Section V. Finally, Section VI concludes the paper.

II. True-Time Delay Beamforming Network

A. Beamforming Network Design

As shown in Fig. 1, the proposed integrated silicon photonic beamforming system modulates a continuous-wave laser signal with the mm-wave signal, and the modulated optical signal propagates through the multiple-output optical circuit. Each optical output is then converted back to the electrical domain by a photodetector and transimpedance amplifier (TIA). Power amplifiers (PAs) follow to drive the antenna array to realize the desired transmit beam pattern. This beam pattern is determined by the group delay between the outputs, which is tuned in a continuous manner via the ORR-based photonic integrated circuit.

Fig. 2(a) shows a single ORR that has one phase shifter for resonance tuning and one MZI coupler for coupling ratio adjustment. Also, a 5% coupled drop port with a Germanium (Ge) waveguide photodetector (PD) is added to the ring for electrical monitoring purposes. Since a single ORR has one feedback path, it can be described as a digital infinite impulse response (IIR) filter whose response repeats with a free spectral range (FSR) period that is determined by the ring circumference. The ORR output magnitude response shows a notch response that is centered at the resonance frequency (f_r), while the monitor magnitude response shows a complementary bandpass response.

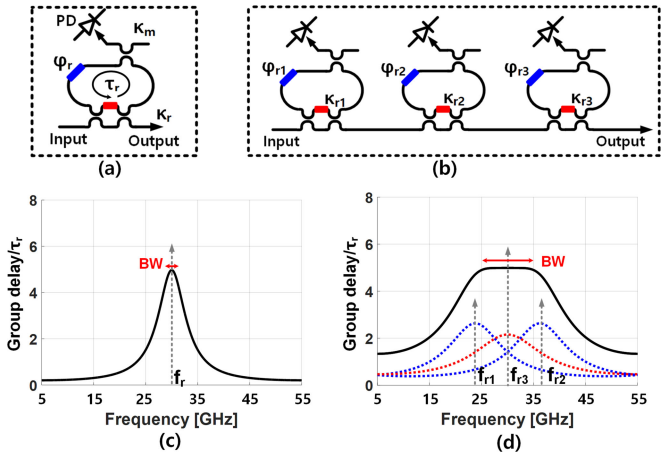

Fig. 2. Schematic of (a) a single ORR and (b) three cascaded ORRs. Simulated normalized group delay responses of (c) a single ORR and (d) three cascaded ORRs centered at 30 GHz. The rings have 50 GHz FSR, 0.65 dB round-trip waveguide loss, and 20 ps round-trip delay.

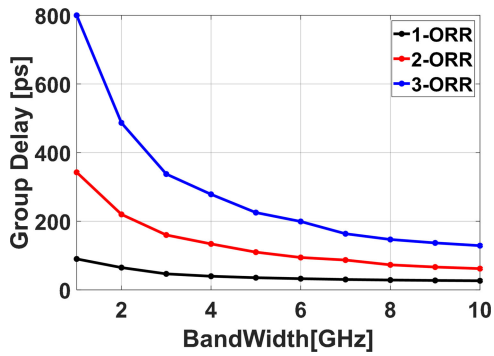

Fig. 3. Simulated group delay versus bandwidth for a varying number of cascaded ORRs. Design conditions are group delay ripple $<$ 1.6 ps, FSR $=$ 50 GHz, and RTL $=$ 0.65 dB.

A single ORR group delay response (τ_g) is

$$\tau_g(f) = \frac{\kappa_r \tau_r}{r(2-\kappa_r) - (1+r^2)\sqrt{1-\kappa_r}\cos(2\pi f \tau_r + \phi_r)}, \quad (1)$$

where ϕ_r is the ring phase shift, κ_r is the ring MZI coupling ratio, τ_r is the round-trip delay, and r is the ring round-trip loss (RTL) [25]. The 2π phase shift limitation in one FSR period of a single ring resonator presents a strong trade-off where increased group delay results in dramatically reduced bandwidth, as shown in Fig. 3 [21]. Therefore, a single ORR can only provide a limited bandwidth-group delay product, which limits its effectiveness for mm-wave signals (Fig 2(c)). This trade-off is broken by cascading multiple rings (Fig 2(b)), as the total group delay response ($\tau_{g,cascaded}$) is the summation of each rings response ($\tau_{g,n}$).

$$\tau_{g,cascaded} = \sum_n \tau_{g,n} \quad (2)$$

Properly setting the coupling ratio ($\kappa_{r1,2,3}$) and resonance of each ring ($f_{r1,2,3}$) allows for an extended bandwidth with a large group delay (Fig. 2(d) and Fig. 3).

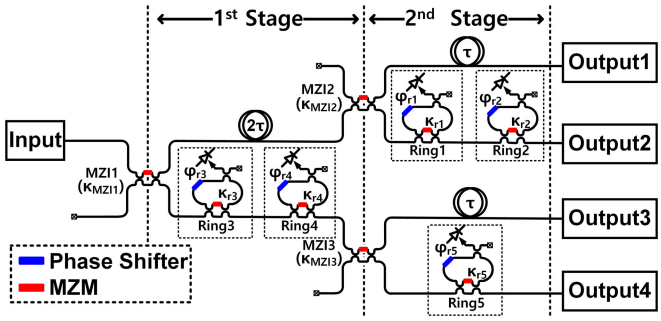

Fig. 4. 1X4 ORR-based asymmetric binary tree OBFN schematic.

One issue with utilizing cascaded ORRs is that passband ripple is present in their combined group delay response, which can cause distortion in the mm-wave signal. Ripple reduction is achieved by adding more ORRs in a given bandwidth, such that their peaks are closer, or by reducing the peak delay [26]. By optimizing the coupling ratios and resonance frequency of each ORR, or by increasing the number of ORRs, this ripple can be reduced to arbitrarily small values [27]. The cascaded ORR group delay response for the targeted bandwidth, group delay, and ripple requirements can be optimized based on three criteria: delay, phase, or signal power [28]. This is done on a per-angle basis to set the optical component values, with the optimization that yields the smallest mean-squared error (ε) from the ideal group delay response (τ_i) utilized.

$$\varepsilon = \int_{BW} (\tau_g(f) - \tau_i)^2 df \tag{3}$$

The beamforming network presented in this paper optimizes the cascaded ring group delay response to allow 1.6 ps ripple over a 2 GHz bandwidth, which corresponds to a phase shift of $\pi/10$ for a 30 GHz signal. This maximum $\pi/10$ phase error degrades array gain by less than 0.5 dB [29].

Several ORR-based OBFNs have been reported, such as symmetrical and asymmetrical parallel structures and symmetrical and asymmetrical binary tree structures [30]. Parallel structures provide large degrees of freedom to generate arbitrary group delay responses. However, they have an increased ring resonator count relative to binary tree structures that share ORRs. Considering linearly increasing group delay requirements in an antenna array, binary tree structures are more efficient than parallel structures for similar group delay performance. Another consideration is symmetrical versus asymmetrical structures. Symmetric structures allow bi-directional beam-angle tuning that covers both negative and positive beam angles. However, they require twice the ORR count as asymmetric designs. A drawback with asymmetric structures is the requirement of an offset delay with additional waveguide length to cover the negative beam angles. However, the lower ORR count provides major reductions in automatic tuning algorithm complexity by reducing the number of tuning elements and the amount of thermal crosstalk. Thus, an asymmetrical binary tree OBFN structure that utilizes the minimum ring count is chosen for the automatic OBFN tuning demonstration.

Fig. 4 shows the 1X4 ORR-based asymmetric binary tree OBFN that was designed in this work. This structure saves

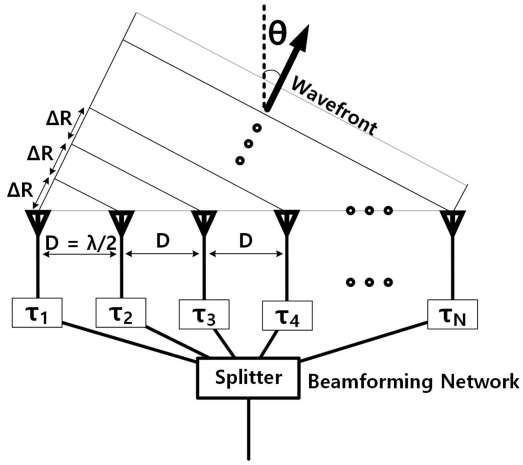

Fig. 5. Conceptual transmitter antenna array with beamforming network.

ORRs by sharing Rings 3 and 4 in the Output 3 and 4 paths. Flexibility in beam tuning angle is achieved by utilizing waveguide delay lines in the design. In order to provide enough group delay response bandwidth, an additional Ring 2 is placed in the Output 2 path. One issue with this structure is that each ORR induces additional loss and each path experiences a different number of ORRs, resulting in different output powers. This output power difference is compensated with tunable couplers (κ_{MZI1-3}) placed at each branch.

The OBFN is designed to work with a 30 GHz ($\lambda \approx 1$ cm) carrier frequency, have 2 GHz bandwidth, and support a beam steering angle of 150° to 210°. Note, this is an identical pattern as −30° to 30° for a linear isotropic antenna array with $\lambda/2$ separation (D) (Fig. 5). For a certain beam radiation angle (θ) at the antenna array, the distance between the same phase wavefront (ΔR) is defined as $\Delta R = D \sin\theta$ and the required delay between the two adjacent OBFN outputs ($\Delta\tau$) is $\Delta\tau = D\cos\theta/c$. In order to meet the specifications, the nominal unit path delay τ is 25.5 ps for the 1X4 OBFN structure. Table I summarizes the delay requirements for the asymmetric binary tree OBFN outputs to cover the targeted beam steering angle range. Assuming 0.65 dB ring round trip loss and designing for a 50 GHz FSR relative to the 1550 nm laser wavelength, Table II summarizes the optical component values extracted from the optimization procedure. A single ORR can provide enough bandwidth for the Output 2 response for radiating angles of 150° to 195°, and thus the Ring 2 coupling ratio is set to zero. However for a radiating angle of 210°, a single ORR with 67.2 ps peak delay cannot provide the required 2 GHz bandwidth. Thus, Ring 2 is activated in cascade with Ring 1 to expand the group delay bandwidth. The simulated OBFN output magnitude and group delay responses for the targeted radiating angles (θ) at the antenna array are shown in Fig. 6. Including MZI1−3 allows for equal output power over the 2 GHz bandwidth for the entire beam angle range.

B. Tuning Algorithm

1) Monitor-Based Single Ring Group Delay Tuning Principle: Tuning of the OBFN involves adjusting each ORRs group delay, which is a function of the rings coupling ratio

TABLE I
OUTPUT GROUP DELAY (WAVEGUIDE + ORR DELAY) REQUIREMENTS FOR CORRESPONDING RADIATING ANGLE AT THE ANTENNA ARRAY

Radiating Angle (θ)	Output 1	Output 2	Output 3	Output 4
$\theta = 150°$	0.0ps (0ps + 0ps)*	25.0ps (-25.5ps + 50.5ps)	50.0ps (-51.0ps + 101.0ps)	75.0ps (-76.5ps + 151.5ps)
$\theta = 165°$	0.0ps (0ps + 0ps)	29.0ps (-25.5ps + 54.5ps)	58.0ps (-51.0ps + 109.0ps)	87ps (-76.5ps + 163.5ps)
$\theta = 180°$	0.0ps (0ps + 0ps)	33.3ps (-25.5ps + 58.8ps)	66.7ps (-51.0ps + 117.7ps)	100.0ps (-76.5ps + 176.5ps)
$\theta = 195°$	0.0ps (0ps + 0ps)	37.6ps (-25.5ps + 63.1ps)	75.3ps (-51.0ps + 126.3ps)	112.9ps (-76.5ps + 189.4ps)
$\theta = 210°$	0.0ps (0ps + 0ps)	41.6ps (-25.5ps + 67.2ps)	83.3ps (-51.0ps + 134.3ps)	124.9ps (-76.5ps + 201.4ps)

*Group delay (path delay + ORR delay)

TABLE II
DESIGNED OBFN COMPONENT VALUES FOR THE CORRESPONDING RADIATING ANGLE (θ) AT THE ANTENNA ARRAY

Radiating Angle (θ)	ORR Coupling Ratio				ORR Phase Shift (rad)					MZI Coupling Ratio		
	κ_{r1}	κ_{r2}	$\kappa_{r3,4}$	κ_{r5}	ϕ_{r1}	ϕ_{r2}	ϕ_{r3}	ϕ_{r4}	ϕ_{r5}	κ_{MZI1}	κ_{MZI2}	κ_{MZI3}
150°	0.810	0	0.680	0.810	3.769	3.769	3.386	4.152	3.769	0.660	0.540	0.570
165°	0.780	0	0.660	0.775	3.769	3.769	3.417	4.121	3.769	0.670	0.545	0.575
180°	0.753	0	0.630	0.750	3.769	3.769	3.445	4.093	3.769	0.680	0.548	0.580
195°	0.728	0	0.595	0.730	3.769	3.769	3.469	4.069	3.769	0.695	0.553	0.590
210°	0.859	0.859	0.580	0.703	3.191	4.347	3.490	4.048	3.769	0.705	0.556	0.595

and phase shift. Each ring employs a tunable MZI coupler and phase shifter to achieve this (Fig. 2(a)). As shown in Fig. 7, the ORR resonance frequency(f_r) is adjusted by tuning the phase shifter (ϕ_r) and the depth of the output port notch response is determined by the coupling ratio (κ_r). The rings monitor port shows a complementary bandpass response with the peak at the same resonance frequency. This relationship is utilized in our previous monitor-based tuning work [31]–[34] to set the desired ORR magnitude response in the presence of deviated coupling ratio and resonance frequency due to process and temperature variations. This approach is modified in this work to allow for monitor-based ORR group delay tuning.

In order to utilize monitor-based tuning, the group delay response should be mapped to the monitor response. As can be seen in Fig. 7, both the ORR group delay and monitor output display similar bell-shaped responses centered at the ORR resonance frequency. Thus, calibrating the monitors peak output will also set the peak of the ORR group delay to the desired frequency. Since the monitor response is maximized when the ORR resonance frequency corresponds to the input laser frequency/wavelength, maximizing the monitor signal while tuning the phase shifter (ϕ_r) allows for tuning the ring to the targeted resonance frequency.

As shown in Fig. 8, decreasing the coupling ratio from a large value monotonically increases the maximum ORR group delay at the resonance frequency until critical coupling is achieved. The rings RTL sets the critical coupling ratio and affects the group delay slope, such that a larger spread is observed as the group delay increases. This necessitates careful characterization of a rings RTL. Note that this work lumps the 5% monitor coupling in the proposed ORR structure as part of the RTL. While the ORR coupling ratio can theoretically be tuned from 0 to 1, process variations of the directional coupler used in the MZI structure prohibit achieving a maximum coupling ratio of 1 and set a practical minimum ORR group delay. Also, the group delay experiences a very steep reduction for values less than critical coupling. Thus, the coupling ratio range is restricted to tune between 0.5 and 0.9 in the presented OBFN design.

Monitor-based ORR coupling ratio tuning [31], [32] is applied to achieve the targeted group delay. A tuning reference point is first set by finding the critical coupling ratio where the monitor response is maximized. The ORR sinusoidal MZI coupler response is then used to tune to the desired coupling ratio [31]. One thing that must be considered is that the MZI coupler tuning shifts the ORRs resonance frequency by half of the phase difference between the two MZI arms [22] and additional frequency shift occurs due to thermal crosstalk. This unwanted resonance shift is compensated by adjusting the ring phase shift (ϕ_r) in parallel to correct the resonance frequency. This tuning procedure is valid for narrowband operation around a nominal center wavelength (1550 nm). Also, due to the wavelength-dependency of the directional coupler, recalibration should be performed to operate at a different resonance frequency.

2) Complete Beamforming Network Tuning Procedure: Based on the single ORR group delay tuning principle, a monitor-based automatic tuning algorithm is proposed to calibrate the complete OBFN response. Fig. 9 shows the flowchart for automatic tuning of a 1X4 OBFN, where each output response is set by individual tuning of a specific ring through monitoring its drop port response. This algorithm is verified in MATLAB utilizing a 1X4 OBFN model and pre-characterized ORR RTL and MZI coupler V_π values.

Step 1 - Output 1 & Output 2 Path Tuning: Process variations cause the optical component values to initially deviate from the designed values in Table II, resulting in significantly distorted responses at the four output ports (Fig. 10(a)). Referring to Fig. 4, the Output 1 and 2 ($\kappa_{r1,2}, \kappa_{MZI1,2}$) paths are calibrated first utilizing the desired center wavelength/frequency laser stimulus (1549.76 nm). This single laser input is split amongst the four outputs through MZI 1, 2 and 3 ($\kappa_{MZI1,2,3}$). Given that it is

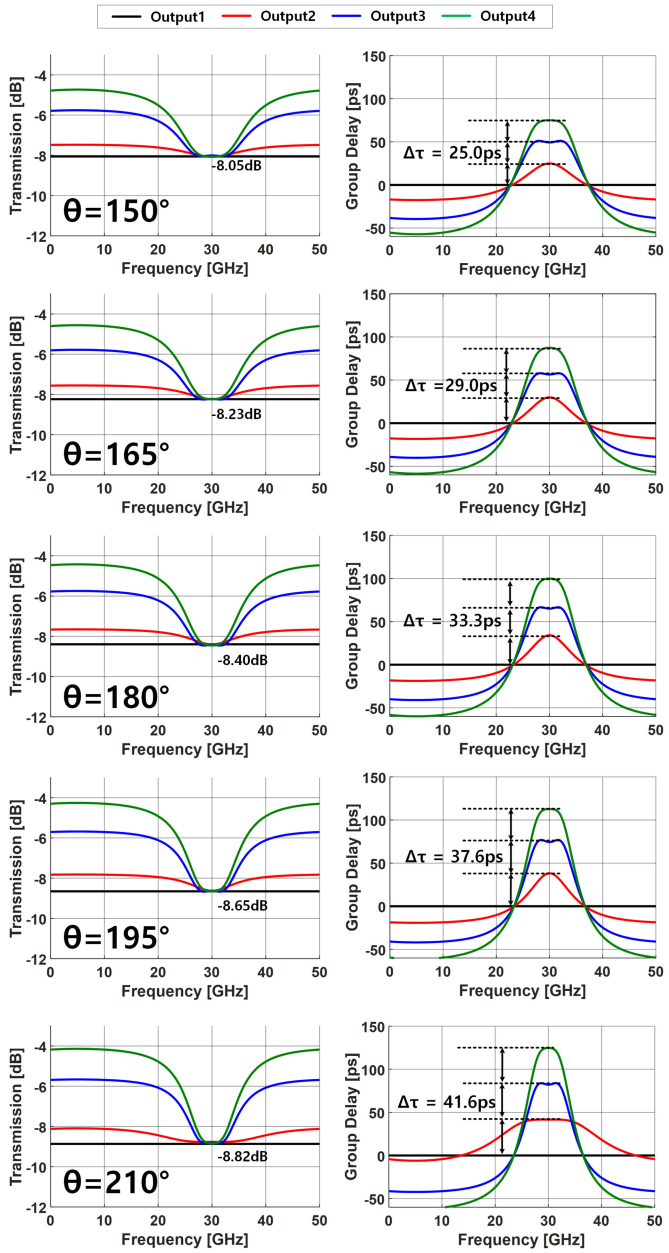

Fig. 6. Simulated OBFN magnitude and group delay response as the radiating angle varies from 150° to 210° from the assumed linear antenna array with isotropic antenna elements.

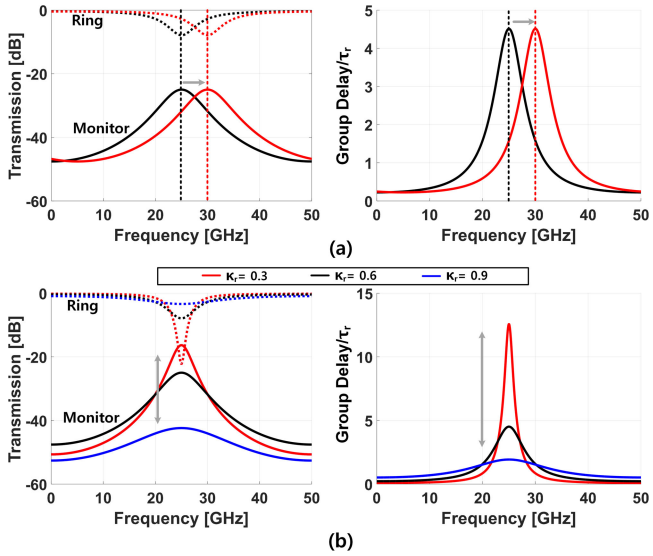

Fig. 7. Simulated ORR output magnitude, monitor, and group delay responses with (a) phase shifter (ϕ_r) tuning and (b) MZI coupler (κ_r) tuning.

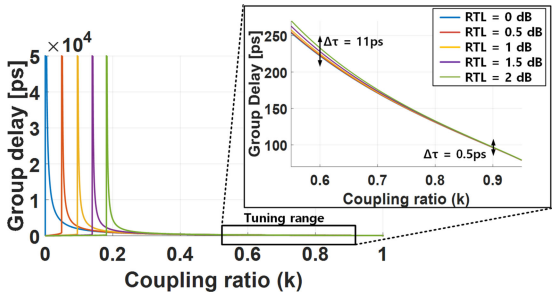

Fig. 8. Simulated single ORR group delay response with different round trip loss values.

important to maximize the monitor SNR in order to improve the coupler tuning accuracy, MZI 1 and 2 are first tuned to maximize the Output 2 power. This is achieved by tuning MZI 1 and 2 to maximize the Monitor 1 response. A coarse-to-fine search algorithm, with an initial 5-bit resolution sweep of the MZI coupler phase shifter across the full range that is followed by a fine 11-bit resolution sweep over the appropriate sub-range, is used to find this maximum point rapidly with 11-bit resolution. During MZI 1 and 2 tuning, the resonance of Ring 1 shifts due to the thermal crosstalk. To correct this error, Ring 1 resonance tuning is performed in parallel with MZI 1 and 2 coupler tuning. After maximizing the Output 2 power and storing $\kappa_{MZI1,2}$, the Ring 1 MZI coupler κ_{r1} is tuned to the critical coupling ratio by maximizing the Monitor 1 signal. A coarse-to-fine search algorithm is also used in this step, along with resonance tuning of Ring 1 being performed in parallel. After saving the Ring 1 critical coupling ratio, the Ring 2 critical coupling ratio is then obtained. Given that Ring 1 and 2 are cascaded in the Output 2 path, the Ring 2 monitor response is affected by the previous Ring 1 response. To address this issue, Ring 1 is tuned to zero coupling by using the saved critical coupling ratio and the MZI sinusoidal characteristic. Then, the Ring 2 MZI coupler is tuned to the critical coupling ratio by maximizing the Monitor 2 response. In parallel, resonance tuning of Ring 2 is performed. After finding both Ring 1 and 2 critical coupling ratios, this reference point and the MZI sinusoidal characteristic is utilized to tune both rings MZI couplers to their desired ratios for a given beam angle. Finally, MZI 2 is tuned to equalize the Output 1 and 2 power using the MZI characteristic. Fig. 10(b) shows the simulated OBFN response after Step 1 for a 150° angle. While Outputs 1 and 2 are now close to the desired group delay and have near equal power, Outputs 3 and 4 are still highly distorted.

Step 2 - Output 3 Path Tuning: The critical coupling values of Rings 3 and 4 in the Output 3 path are obtained in this step. Following the same procedure as Step 1, MZI 1 is first tuned to

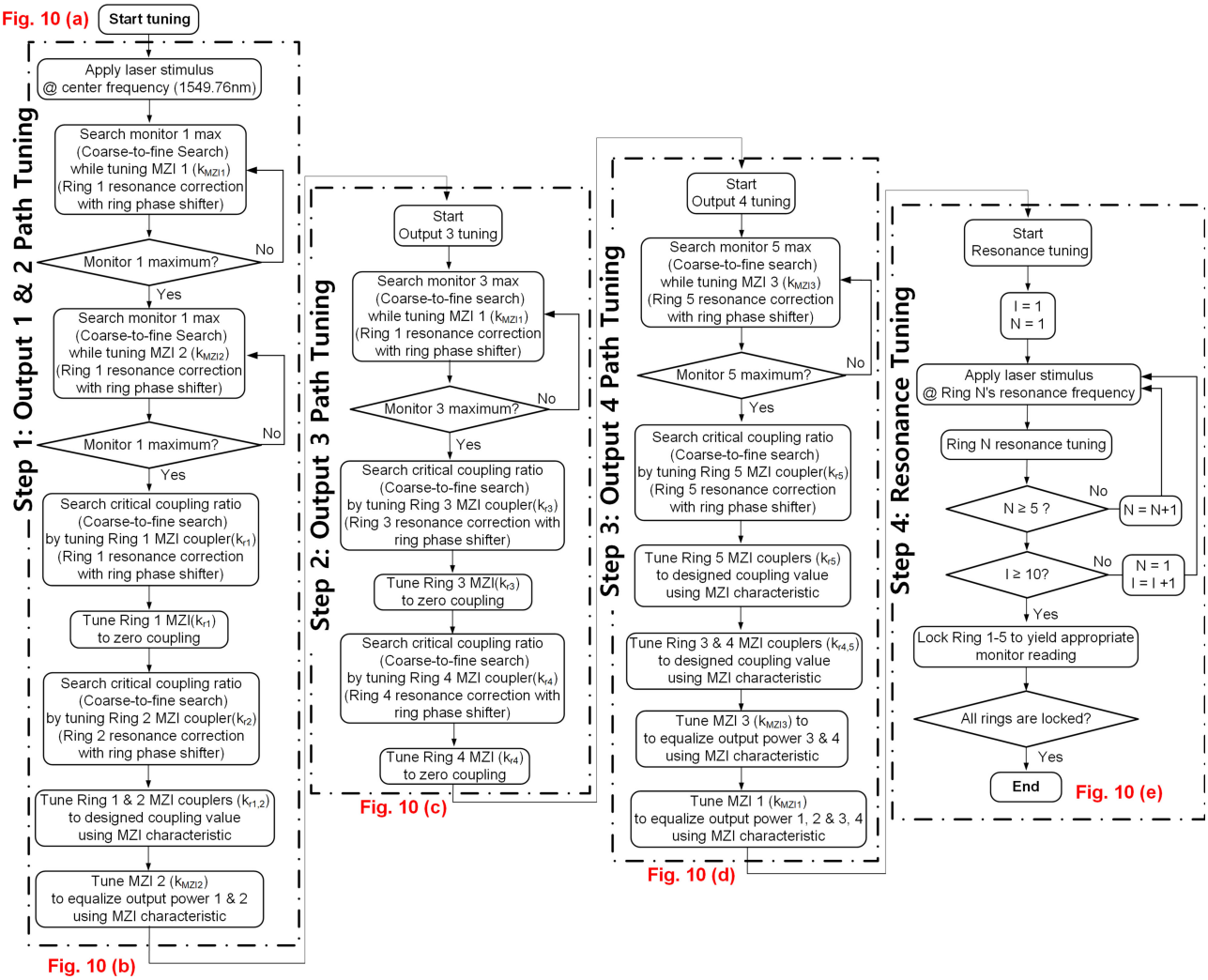

Fig. 9. 1X4 OBFN calibration algorithm flowchart.

maximize the Monitor 3 and 4 readings. Note that since Rings 3 and 4 are placed before MZI 3, the tuning of this MZI is not necessary. The Ring 3 and 4 MZI couplers are then tuned to find the critical coupling settings. Similar to Step 1, the Ring 3 MZI coupler is tuned to zero coupling temporarily during the Ring 4 coupler tuning. After obtaining the critical coupling values of Ring 3 and 4, both of the ORRs coupling ratios are then tuned to zero coupling in order to tune Ring 5 in the next step. Fig. 10(c) shows the simulated OBFN response after this intermediate Step 2, with the Output 3 group delay response now showing a flat response due to both Rings 3 and 4 coupling ratios being set to zero coupling in preparation for Step 3. Also, note that the Ring 2 center frequency has shifted due to thermal cross-talk and must be corrected later.

Step 3 - Output 4 Path Tuning: The critical coupling values of Ring 5 in the Output 4 path are obtained in this step, along with setting the desired coupling ratios of Rings 3–5 and optimizing the MZI 1 and 3 coupling values. First, MZI 3 is tuned to maximize the Monitor 5 reading for accurate calibration. Then, the Ring 5 MZI critical coupling ratio is obtained by maximizing the Monitor 5 signal. Now that the critical coupling values of Rings 3–5 have been stored, these coupling ratios are then adjusted to the desired values using the MZI sinusoidal characteristic. Finally, MZI 1 and 3 are tuned to the desired values to equalize the whole OBFN output powers. Fig. 10(d) shows the simulated OBFN response after Step 3. While the output powers are now closer, they are not exactly the same and the group delays are still off due to the rings resonance frequencies not being set to their final values.

Step 4 - Resonance Tuning: The final step is OBFN resonance tuning to set the group delay center frequency and bandwidth. Rings 1–5 are resonance tuned in order by adjusting the individual rings phase shifter (ϕ_{r1-5}) to maximize the monitor reading with the laser input wavelength/frequency switched to the corresponding ideal f_r. Since resonance tuning is sensitive to thermal crosstalk, multiple iterations are performed across the rings. Note that this is different than the MZI coupler coefficient tuning procedure that is relatively robust to the thermal cross-talk due to any temperature change being common to both arms [35]. Fig. 10(e) shows that after this final tuning step the

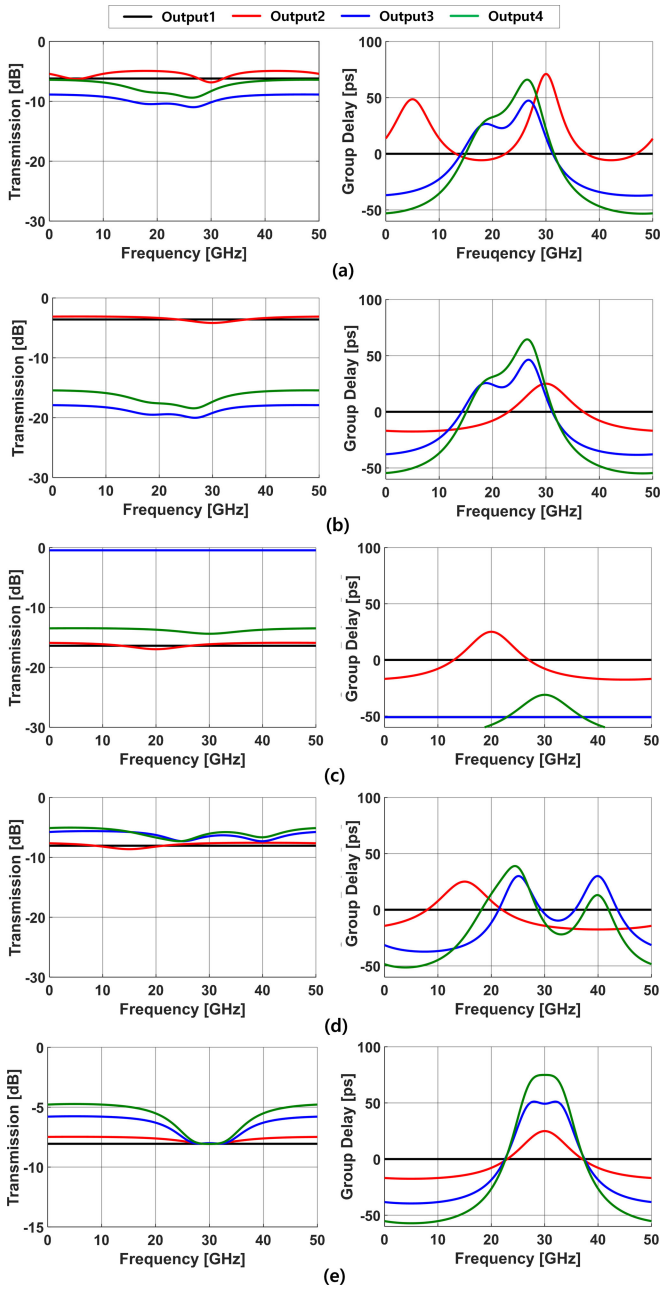

Fig. 10. Simulated OBFN output transmission and group delay responses for a radiating angle of 150° at the antenna array. (a) The initial response with process variations. (b) After Output 1 & 2 tuning. (c) After Output 3 tuning. (d) After Output 4 tuning. (e) After ring resonance tuning.

OBFN's four outputs have well-defined group delay responses and equalized power around the 30 GHz center frequency.

III. Device Design and Fabrication

The presented automatic OBFN tuning algorithm is demonstrated using a 1X4 asymmetric binary tree structure fabricated in the IME A*STAR baseline Si photonics process that utilizes SOI wafers. As shown in the die micrograph of Fig. 11(a), the OBFN structure occupies 4575 μm $\times$ 800 μm. Rib waveguides are employed to minimize propagation loss. They are designed with a 220 nm total slab height, that has a 90 nm thick partially-etched strip, and a 500 nm width silicon core surrounded by SiO_2 cladding (Fig. 11(b)). In order to achieve a nominal unit delay (τ) of 25.5 ps, 1981.4 μm additional waveguide length is added to the appropriate paths. 1-D grating couplers with a center frequency around 1550 nm are placed at the OBFN input and output ports. The OBFN's ORRs are designed with 1554 μm ring circumference to achieve a 50 GHz FSR and have a rounded rectangular shape with 25 μm radius corners to minimize area and waveguide propagation loss. The ORR drop port monitors are designed for 5% coupling and are terminated with waveguide Ge p-i-n PDs. N-doped thermo-optic phase shifters are implemented 0.6 μm away from the sidewall of the waveguide slab to minimize optical loss. These thermal phase shifters provide ORR resonance tuning over a full FSR at a maximum 87 mW power. Directional couplers with a 200 nm gap are employed throughout the OBFN structure, with the couplers in the tunable MZI structures having a nominal 50% coupling ratio. The MZI coupler heaters require a maximum 125 mW to tune the coupling ratio over the utilized range. Metal bondpads are placed at the top and bottom edges of the photonic integrated circuit (PIC) to electrically control the phase shifter heaters and provide the bias and electrically monitor the drop-port PD signals. In order to reduce the amount of thermal crosstalk between the thermo-optic phase shifters, the default silicon substrate thickness of 750 μm is thinned to 75 μm with an additional CMP process. This reduces the thermal time constant and results in a dramatic improvement in tuning speed [31].

IV. Experimental Results

A. Measurement Setup

The OBFN automatic monitor-based tuning system block diagram and a picture of the measurement setup is shown in Fig. 12. A free-space optical fiber coupling stage couples a tunable laser (Luna Phoenix 1400) into the PIC. This tunable laser generates the five wavelengths required for calibration that correspond to each ORR resonance. The PIC is wire-bonded to the custom-designed printed circuit board (PCB) that includes low-bandwidth transimpedance amplifiers (TIAs) using op-amps (OPA727) and 12-bit analog-to-digital converters (ADCs) (Arduino Due internal ADC) to sense the average photocurrent from the OBFN ORR's monitor waveguide Ge PDs that are biased at -1 V. These ADCs interface with a microcontroller (Arduino Due) that implements the OBFN tuning algorithm by controlling 16-bit digital-to-analog converters (DACs) (LTC2668) through a serial peripheral interface (SPI). The DACs apply control voltages across the resistive heaters on the PIC to adjust the optical phase shifters. A fully-automated tuning system is achieved with the tunable laser also controlled by the same microcontroller. The PIC is placed on a large metal footprint with thermal vias down to the bottom layer of the PCB where a thermoelectric cooler (TEC) is placed with thermal grease passivation to provide temperature stabilization.

An optical vector network analyzer (OVNA) signal is coupled into the PIC for device characterization and verification of the calibrated OBFN group delay and magnitude responses.

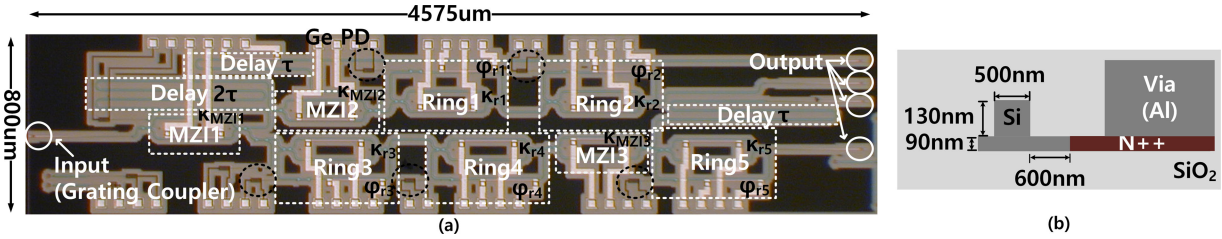

Fig. 11. (a) OBFN chip micrograph. (b) Cross-section schematic of the rib waveguide with resistive heater.

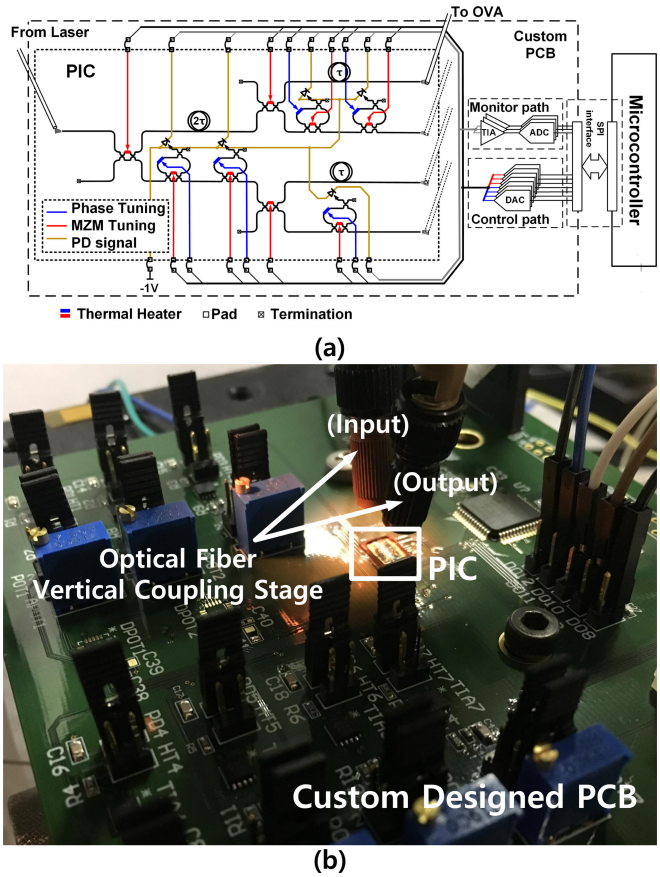

Fig. 12. Automatic monitor-based tuning system. (a) Block diagram with the OBFN. (b) Photograph of the system with the optical fiber vertical coupling stage.

The OBFN output group delay responses are obtained using the OVNA time domain response at the corresponding outputs. Since group delay is sensitive to noise, digital filtering over 40 samples and time domain windowing are used [36]. Each ORR in the OBFN structure is characterized independently by configuring zero coupling for the other rings. A Jones matrix method that employs a time domain impulse response of the ORR and its corresponding transfer function is utilized to extract accurate RTL values. From the ORR's Jones matrix [37], a 0.65 dB (±0.1 dB) RTL and 0.3963 nm (49.64 GHz) FSR is determined. These characterized round trip loss measurements are used to determine the ORR critical coupling values and to model the group delay response.

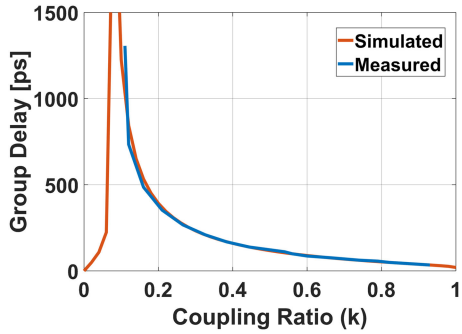

Fig. 13. Measured single ORR group delay response vs coupling ratio.

B. Single ORR Measurement

Accurate OBFN automatic tuning requires initial characterization of the ORRs. To characterize a specific ring resonator, the other cascaded ring resonators' coupling ratio are set to zero to remove their response seen at the output. One issue is that the ORR resonance drifts slightly when tuning the coupler due to the varying phase shift of the MZI coupler and thermal crosstalk [22]. This is compensated by performing resonance tuning in parallel with the ORR coupler tuning [31]. Fig. 13 shows the measured ORR group delay response versus ORR coupling ratios, which shows good agreement with simulations utilizing 0.65 dB round-trip loss. Theoretically, the ORR coupling ratio can vary from 0 to 1 by tuning the thermal phase shifter (κ_r) of the corresponding MZI coupler. However, fabrication variations of the 50% couplers present in the MZI coupler limit the coupling ratio tuning range to a maximum of 0.93. Neglecting the dramatically-changing group delay region with low coupling ratios, this limits the minimum achievable OBFN group delay response to 34.5 ps. Overall, the good agreement between the measured and simulated group delay response versus coupling ratio validates that the monitor-based tuning approach can precisely set a desired group delay during the full OBFN tuning procedure.

C. Full OBFN Tuning

The proposed OBFN tuning algorithm is demonstrated with the 1X4 asymmetric binary tree OBFN structure. Fig. 14 shows that the fabricated devices initial output responses have significant variation in output magnitude and severely deviate from the designed group delay responses. Recovery from this initial poor response is possible due to all of the ring phase shifters having

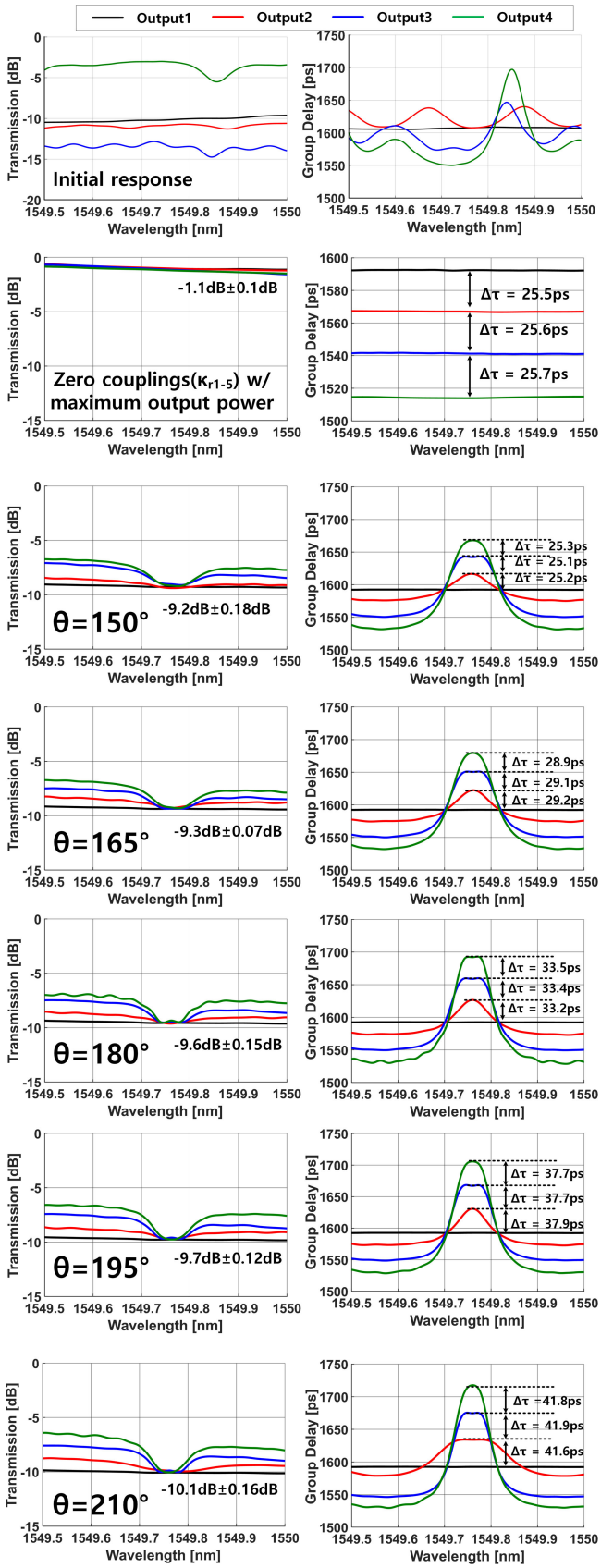

Fig. 14. Measured 1X4 OBFN magnitude and group delay responses for an initial un-tuned setting, a flat configuration with maximum output power, and as the radiating angle varies from 150° to 210°.

TABLE III
INPUT LASER WAVELENGTHS UTILIZED IN FULL OBFN TUNING

Radiating Angle(θ)	Wavelength (nm)				
150°	1549.76	1549.784	1549.735		
165°	1549.76	1549.782	1549.737		
180°	1549.76	1549.781	1549.739		
195°	1549.76	1549.779	1549.740		
210°	1549.76	1549.775	1549.742	1549.797	1549.723

a full FSR tuning range and the tunable MZI couplers providing a wide tunable coupling ratio from 0.5 to 0.9. Before tuning to a specific angle, the OBFN path delays are first characterized by setting all the ORR coupling ratios to zero and maximizing the output power by tuning the MZI couplers ($\kappa_{MZI1,2,3}$). OVNA measurements show that, after normalizing for 9 dB of input/output grating coupler insertion losses, the OBFN displays 1.1 dB of combined tunable coupler and waveguide propagation loss (Fig. 14). This magnitude response varies by ±0.1 dB due to grating coupler fabrication variations, fiber alignment error, and limitations in the achievable MZI coupler ratios. These MZI coupler limitations, which are due to the 50% directional coupler imperfections, are corrected through the coupler tuning algorithm [32], [33]. The measured group delays of the output paths display close to the nominal 25.5 ps spacing.

Utilizing the 1549.76 nm center wavelength (30 GHz away from 1550 nm) and four additional wavelengths (Table III) derived from the tunable laser, the OBFN tuning algorithm is applied and well-defined group delay responses are observed as the angle is tuned from 150° to 210° (Fig. 14). The calibrated OBFN group delay responses show errors less than ±0.3 ps, with the smallest 2.02 GHz (16.2 pm) bandwidth occurring at Output 2 with a 195° radiating angle. For a given angle, the proposed algorithm equalizes the output power levels to have less than ±0.2 dB variation. For different radiating angles, the mean output power level can vary by 0.9 dB due to the innate characteristic of the ORR based OBFN. This correlated output variation could potentially be compensated through subsequent TIA and PA gain control in the electrical domain. Note that only the largest 210° angle requires all five input tuning wavelengths due to this angles group delay values requiring activation of Ring 2. All the other angles have zero coupling for Ring 2 and only require three tuning wavelengths.

Further insight on the measured OBFN group delay responses is possible by simulating the radiating beam patterns of a 4 element linear isotropic antenna array in MATLAB. An ideal system is assumed at each OBFN output port, with a single PD that down-converts the optical signal to a mm-wave photocurrent this is amplified by a TIA and PA for driving an antenna array element. Utilizing a single PD per OBFN output port for the optical-to-electrical down-conversion allows for operation independent of the exact phase of the carrier laser, and thus no carrier tuning is required. As shown in Fig. 15, the linear array has 5mm spacing and operates over a 29–31 GHz frequency band with good agreement in main lobe directionality

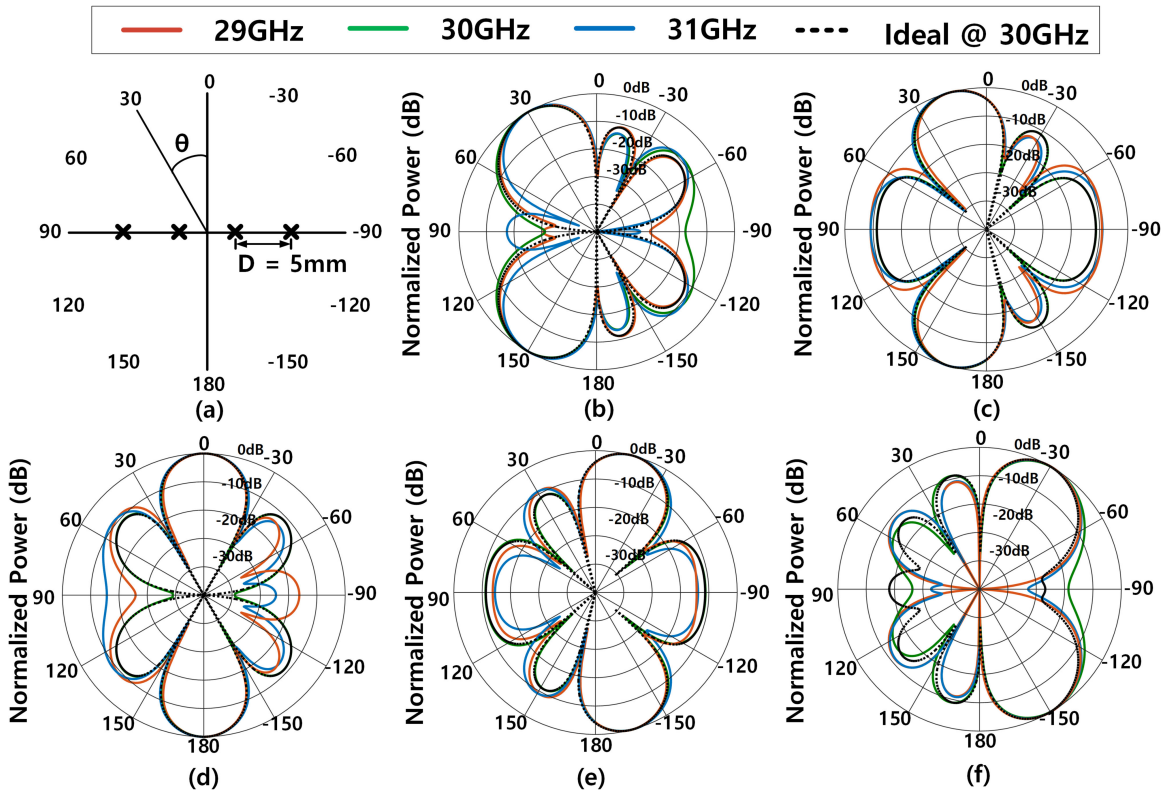

Fig. 15. Simulated linear array beam patterns based on measured automatically-tuned OBFN output responses. (a) Assumed linear array. Radiating angles at (b) 150° (30°), (c) 165° (15°), (d) 180° (0°), (e) 195° (−15°), and (f) 210° (−30°).

and power within 0.1 dB of the ideal OBFN response. While the sidelobes are slightly increased relative to the ideal case due to the group delay ripple and residual magnitude error, the main lobe maintains at least a 9.5 dB larger response over the maximum sidelobe for all angles. The true time-delay operation of the ORRs allows for squint-free operation, with the same radiating angle achieved over the 29–31 GHz band.

For each radiating angle, the OBFN automatic tuning process involves the calibration of 13 heaters for ORR and MZI coupler tuning and takes 1617s to complete. The coarse-to-fine search algorithm employed in the MZI coupler and ORR resonance tuning makes the convergence time somewhat independent of the initial response. As shown in the measured DAC plots for a 210° radiating pattern (Fig. 16), each of the four tuning steps shows good convergence. This is achieved by tuning the corresponding ring phase shifter in parallel to track the monitor reading during the MZI coupler tuning procedure. The average tuning power dissipation for this 210° setting is 862 mW. The individual DAC codes are stored for each radiating angle during this initial calibration procedure. Subsequent rapid switching between the different angles is achieved by simply recalling these stored DAC codes, with this process only limited by the 300 ms measured heater cooling time that is set by the TEC feedback loop [31].

V. Discussion

Table IV summarizes the integrated silicon photonic OBFN performance and compares it with other implementations. This work targeted a potential 5G application that utilizes a 30 GHz carrier frequency and achieves a higher RF bandwidth than the other asymmetric binary tree design [21]. Relative to the ORR-based symmetric binary tree design [22], it utilizes fewer ORRs. Also, the proposed OBFN allows for continuous tuning at a much higher resolution than the 4-bit delay line implementation [38]. Overall, the presented approach is the first and only design to offer fully automatic calibration of the OBFN group delay response and output power.

There are several areas of improvement possible in future implementations of the proposed OBFN. The current design has a single ORR minimum achievable group delay response that is limited to 34.5 ps, while the path delay is designed at 25.5 ps. In order to achieve the −30° to 30° radiating angles at the antenna array, large group delay responses are set at the cost of some bandwidth. Considering the minimum group delay requirements, this can be improved by simply increasing the path delay to 43 ps. This will extend the OBFN bandwidth by 36% by reducing the required ORR group delay from 201.5 ps to 142.9 ps. Another observation is that $\tau_{output4} > \tau_{output3} > \tau_{output2} > \tau_{output1}$ for the asymmetric binary tree OBFN structure to cover the same radiating angle at the antenna (Table I). This design achieved this with more identical ORRs in a particular path to achieve a larger delay. In order to have a larger bandwidth, the ORRs can be further optimized by varying their size for the different output paths. Also, one practical limitation of the current demonstration is that the output grating couplers were not designed to accommodate an output fiber array. This resulted in inefficient measurement procedures and some output power variance due to alignment errors. Aligning the output grating couplers with a standard fiber array spacing will improve this and ease the electrical connection in a full transmitter demonstration.

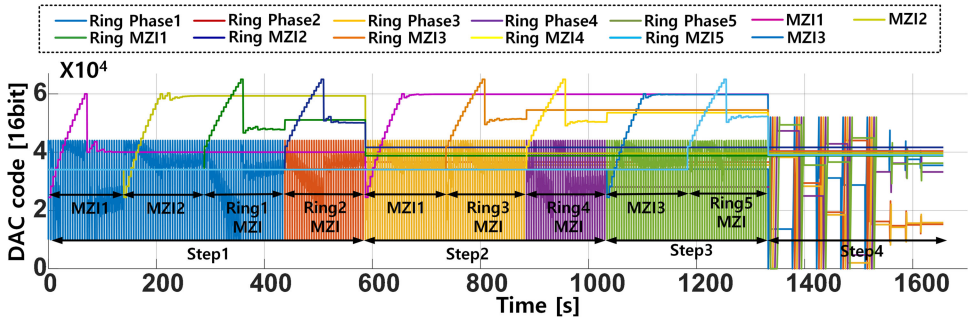

Fig. 16. 1X4 OBFN automatic tuning convergence for a 210° radiating pattern.

TABLE IV
INTEGRATED OBFN COMPARISON TABLE

	This work	[21]	[22]	[38]
Operating Frequency	29 - 31GHz	10.7 - 12.75GHz	75 - 100GHz	-
Platform	SOI	Silicon Nitride (TriPleX)	Silicon Nitride	Silicon Nitride
Laser Wavelength	1550nm	1550nm	1550nm	1550nm
OBFN Type	TX	RX	TX	TX
Input×Output	1×4	8×1	1×4	2×2
Delay Element	5 ORR	8 ORR	8 ORR	Delay line + Swtich
FSR	50GHz	15GHz	22GHz	-
Structure	Asymmetric binary tree	Asymmetric binary tree	Symmetric binary tree	Swtch matrix
Tuning Resolution	Continuous	Continuous	Continuous	4 bit
Delay Range	36 - 200 (ps)	40 - 600 (ps)	8.7 - 209 (ps)	0 - 12.35 (ns)
RF Bandwidth	2GHz	1GHz	6GHz	-
Automatic Calibration	Y	N	N	N

Other important issues are OBFN insertion loss and thermal crosstalk amongst the tuning elements. In order to have sufficient SNR for the monitor-based tuning approach, 5% coupled drop port monitors are added in the OBFN structure. This increases the round trip loss of each ring resonator by an additional 0.22 dB, resulting in an additional total OBFN transmission loss and RF link gain reduction of 0.84 dB. Implementing transparent detectors, such as a contactless integrated photonic probe (CLIPP) [39], can potentially remove this penalty. Thermal crosstalk between the heaters limited OBFN calibration time and resulted in complex tuning steps. Reduction in this thermal crosstalk is possible with more thermally-efficient heater designs utilizing graphene [40], tungsten [41], chromium [42], and resistive heaters directly doped on the waveguide [41], [43]. Also, optimizing the size and shape of the heaters, placing thermal isolation [44], or employing compact cooler packaging (μ-TEC) [45] can provide further improvements in both thermal crosstalk and tuning efficiency.

Finally, while only the OBFN was implemented at the PIC level and a tunable laser was used to generate the five different calibration wavelengths, there is the potential for a more efficient tightly-integrated system. As shown in Fig. 1, the input E-O conversion MZM, image rejection filter, and OBFN with output O-E conversion photodetectors can be integrated as a single PIC and mounted on a custom-designed PCB board. Employing flip-chip bonding of a CMOS chip, which includes the tuning control circuitry and TIAs and PAs to condition the OBFN outputs to drive the antenna elements, would allow for low interconnect parasitics to achieve high frequency operation. With this integrated solution, only a single wavelength laser source is required for calibration, since this laser can be modulated via the input MZM with five different mm-wave frequency signals from a frequency synthesizer on the CMOS chip. This, in combination with the image rejection filter, would generate tones corresponding to the required tuning wavelengths. It is envisioned that an external separately-packaged single-wavelength laser module would be utilized to allow for better thermal management. This laser output would be routed with a single-mode fiber and into the OBFN PIC via a grating coupler.

VI. CONCLUSION

This paper has presented an automatic monitor-based calibration scheme for a silicon photonic ORR-based asymmetric binary tree OBFN. Utilizing electrical information obtained from monitor photodetectors at the ORRs' drop ports, the proposed tuning algorithm compensates fabrication variations and thermal crosstalk by controlling individual micro-heaters. Successfully calibration of a 1X4 OBFN from a severely degraded initial response to the well-defined group delay responses required for a targeted radiating angle over 60° in a linear beamforming antenna array is achieved. Overall, leveraging the proposed automatic calibration scheme can allow for robust operation of OBFNs in future wideband wireless communication systems.

REFERENCES

[1] A. Ghosh *et al.*, "Millimeter-wave enhanced local area systems: A high-data-rate approach for future wireless networks," *IEEE J. Sel. Areas Commun.*, vol. 32, no. 6, pp. 1152–1163, Jun. 2014.

[2] R. Waterhouse and D. Novack, "Realizing 5G: Microwave photonics for 5G mobile wireless systems," *IEEE Microw. Mag.*, vol. 16, no. 8, pp. 84–92, Sep. 2015.

[3] D. Jenn, Y. Loke, M. Tong, E. C. Yeo, and R. Broadston, "Distributed phased arrays with wireless beamforming," *Proc. Conf. Rec. 41st Asilomar Conf. Signals, Syst. Comput.*, 2007, pp. 948–952.

[4] D.-W. Kang, J.-G. Kim, B.-W. Min, and G. M. Rebeiz, "Single and four-element Ka-band transmit/receive phased-array silicon RFICs with 5-bit amplitude and phase control," *IEEE Trans. Microw. Theory Techn.*, vol. 57, no. 12, pp. 3534–3543, Dec. 2009.

[5] K.-J. Koh and G. M. Rebeiz, "An x-and ku-band 8-element phased-array receiver in 0.18-μm SiGe BiCMOS technology," *IEEE J. Solid-State Circuits*, vol. 43, no. 6, pp. 1360–1371, Jun. 2008.

[6] J. Capmany and D. Novak, "Microwave photonics combines two worlds," *Nature Photon.*, vol. 1, no. 6, pp. 319–330, 2007.

[7] D. Marpaung, C. Roeloffzen, R. Heideman, A. Leinse, S. Sales, and J. Capmany, "Integrated microwave photonics," *Laser & Photon. Rev.*, vol. 7, no. 4, pp. 506–538, 2013.

[8] J. Yao, "Microwave photonics," *J. Lightw. Technol.*, vol. 27, no. 3, pp. 314–335, 2009.

[9] W. Ng, A. A. Walston, G. L. Tangonan, J. J. Lee, I. L. Newberg, and N. Bernstein, "The first demonstration of an optically steered microwave phased array antenna using true-time-delay," *J. Lightw. Technol.*, vol. 9, no. 9, pp. 1124–1131, 1991.

[10] R. D. Esman *et al.*, "Fiber-optic prism true time-delay antenna feed," *IEEE Photon. Technol. Lett.*, vol. 5, no. 11, pp. 1347–1349, Nov. 1993.

[11] A. Molony, C. Edge, and I. Bennion, "Fibre grating time delay element for phased array antennas," *Electron. Lett.*, vol. 31, no. 17, pp. 1485–1486, 1995.

[12] H. Zmuda, R. A. Soref, P. Payson, S. Johns, and E. N. Toughlian, "Photonic beamformer for phased array antennas using a fiber grating prism," *IEEE Photon. Technol. Lett.*, vol. 9, no. 2, pp. 241–243, Feb. 1997.

[13] J. Roman, M. Frankel, P. Matthews, and R. Esman, "Time-steered array with a chirped grating beamformer," *Electron. Lett.*, vol. 33, no. 8, pp. 652–653, 1997.

[14] B. Howley, X. Wang, M. Chen, and R. T. Chen, "Reconfigurable delay time polymer planar lightwave circuit for an x-band phased-array antenna demonstration," *J. Lightw. Technol.*, vol. 25, no. 3, pp. 883–890, 2007.

[15] W. Ng, D. Yap, A. Narayanan, and A. Walston, "High-precision detector-switched monolithic GaAs time-delay network for the optical control of phased arrays," *IEEE Photon. Technol. Lett.*, vol. 6, no. 2, pp. 231–234, Feb. 1994.

[16] K. Horikawa, I. Ogawa, H. Ogawa, and Tsutomu Kitoh, "Silica-based integrated planar lightwave true-time-delay network for microwave antenna applications," in *Proc. Opt. Fiber Commun. Conf.*, 1996, Paper WB4.

[17] F. Xia, L. Sekaric, and Y. Vlasov, "Ultracompact optical buffers on a silicon chip," *Nature Photon.*, vol. 1, no. 1, pp. 65–71, 2007.

[18] J. Cardenas *et al.*, "Wide-bandwidth continuously tunable optical delay line using silicon microring resonators," *Opt. Express*, vol. 18, no. 25, pp. 26 525–26 534, 2010.

[19] J. Xie, L. Zhou, Z. Zou, J. Wang, X. Li, and J. Chen, "Continuously tunable reflective-type optical delay lines using microring resonators," *Opt. Express*, vol. 22, no. 1, pp. 817–823, 2014.

[20] N. Tessema *et al.*, "Radio beam-steering via tunable Si3N4 optical delays for multi-Gbps K-band satellite communication," in *Proc. Opt. Fiber Commun. Conf.*, 2016, Paper W3K-4.

[21] L. Zhuang *et al.*, "Novel ring resonator-based integrated photonic beamformer for broadband phased array receive antennas–part II: Experimental prototype," *J. Lightw. Technol.*, vol. 28, no. 1, pp. 19–31, 2010.

[22] Y. Liu *et al.*, "Tuning optimization of ring resonator delays for integrated optical beam forming networks," *J. Lightw. Technol.*, vol. 35, no. 22, pp. 4954–4960, Nov. 2017.

[23] X. Wang, L. Zhou, R. Li, J. Xie, L. Lu, and J. Chen, "Nanosecond-range continuously tunable silicon optical delay line using ultra-thin silicon waveguides," in *Proc. CLEO: Science and Innovations*, Optical Society of America, Paper STu1G-5, 2016, pp. STu1G-5, 2016.

[24] G. Choo, C. Madsen, S. Palermo, and K. Entesari, "Ring resonator based integrated optical beam forming network with true time delay for mmW communications," in *Proc. IEEE MTT-S Int. Microw. Symp.*, 2018, pp. 443–446.

[25] O. Schwelb, "Transmission, group delay, and dispersion in single-ring optical resonators and add/drop filters-a tutorial overview," *J. Lightw. Technol.*, vol. 22, no. 5, pp. 1380–1394, 2004.

[26] G. Lenz, B. Eggleton, C. K. Madsen, and R. Slusher, "Optical delay lines based on optical filters," *IEEE J. Quantum Electron.*, vol. 37, no. 4, pp. 525–532, Apr. 2001.

[27] A. Meijerink *et al.*, "Novel ring resonator-based integrated photonic beamformer for broadband phased array receive antennas–part I: Design and performance analysis," *J. Lightw. Technol.*, vol. 28, no. 1, pp. 3–18, 2010.

[28] R. Blokpoel, A. Meijerink, L. Zhuang, C. Roeloffzen, and W. van Etten, "Staggered delay tuning algorithms for ring resonators in optical beam forming networks," in *Proc. 12th IEEE/LEOS Symp. Benelux*, 2007, pp. 243–246.

[29] O. Bakr and M. Johnson, "Impact of phase and amplitude errors on array performance," EECS Dept., Univ. California, Berkeley, CA, USA, Tech. Rep. UCB/EECS-2009-1, 2009.

[30] M. Burla, "Advanced integrated optical beam forming networks for broadband phased array antenna systems," Ph.D. dissertation, Univ. Twente, Enschede, The Netherlands, 2013.

[31] G. Choo, S. Cai, B. Wang, C. K. Madsen, K. Entesari, and S. Palermo, "Automatic monitor-based tuning of reconfigurable silicon photonic APF-based pole/zero filters," *J. Lightw. Technol.*, vol. 36, no. 10, pp. 1899–1911, 2018.

[32] G. Choo, S. Cai, B. Wang, C. Madsen, K. Entesari, and S. Palermo, "Automatic monitor-based tuning of reconfigurable silicon photonic 2nd-order APF-based pole/zero filters," in *Proc. CLEO: Science Innovations*, 2017, Paper SF1H-3.

[33] S. Cai, G. Choo, B. Wang, K. Entesari, and S. Palermo, "Comprehensive adaptive tuning of silicon RF photonic filters," in *Proc. Texas Symp. Wireless Microw. Circuits Syst.*, pp. SF1H-3, 2016.

[34] G. Choo, C. Madsen, K. Entesari, and S. Palermo, "A reconfigurable silicon photonic 4 th-order filter for synthesizing butterworth, chebyshev, and elliptic responses," in *Proc. IEEE Avionics Vehicle Fiber-Opt. Photon. Conf.*, 2017, pp. 15–16.

[35] J. C. Mak, A. Bois, and J. K. Poon, "Programmable multiring butterworth filters with automated resonance and coupling tuning," *IEEE J. Sel. Topics Quantum Electron.*, vol. 22, no. 6, pp. 232–240, Nov./Dec. 2016.

[36] L. Inovations, "Calculating group delay and chromatic dispersion from ova optical phase," 2013. [Online]. Available: http://lunainc.com/wp-content/uploads/2013/06

[37] J. Kim, W. J. Sung, O. Eknoyan, and C. K. Madsen, "Linear photonic frequency discriminator on As2S3-ring-on-Ti:LiNbO3 hybrid platform," *Opt. Express*, vol. 21, no. 21, pp. 24 566–24 573, 2013.

[38] R. L. Moreira *et al.*, "Integrated ultra-low-loss 4-bit tunable delay for broadband phased array antenna applications," *IEEE Photon. Technol. Lett*, vol. 25, no. 12, pp. 1165–1168, Jun. 2013.

[39] F. Morichetti *et al.*, "Non-invasive on-chip light observation by contactless waveguide conductivity monitoring," *IEEE J. Sel. Topics Quantum Electron.*, vol. 20, no. 4, pp. 292–301, Jul./Aug. 2014.

[40] D. Schall *et al.*, "Infrared transparent graphene heater for silicon photonic integrated circuits," *Opt. Express*, vol. 24, no. 8, pp. 7871–7878, 2016.

[41] A. Masood *et al.*, "Comparison of heater architectures for thermal control of silicon photonic circuits," in *Proc. IEEE 10th Int. Conf. Group IV Photon.*, 2013, pp. 83–84.

[42] R. Amatya *et al.*, "Low power thermal tuning of second-order microring resonators," in *Proc. Conf. Lasers Electro-Opt.*, May 2007, Paper CFQ5.

[43] J. E. Cunningham *et al.*, "Highly-efficient thermally-tuned resonant optical filters," *Opt. Express*, vol. 18, no. 18, pp. 19 055–19 063, Aug. 2010. [Online]. Available: http://www.opticsexpress.org/abstract.cfm?URI=oe-18-18-19055

[44] P. Dong *et al.*, "Low power and compact reconfigurable multiplexing devices based on silicon microring resonators," *Opt. Express*, vol. 18, no. 10, pp. 9852–9858, 2010.

[45] R. Enright, S. Lei, G. Cunningham, I. Mathews, R. Frizzell, and A. Shen, "Integrated thermoelectric cooling for silicon photonics," *ECS J. Solid State Sci. Technol.*, vol. 6, no. 3, pp. N3103–N3112, 2017.

Gihoon Choo (S'17) received the B.S. degree in electrical engineering from Seoul National University, Seoul, South Korea, in 2011, and the M.S. and Ph.D. degrees from Texas A&M University, College Station, TX, USA, in 2013 and 2018, respectively. He is a Hardware Engineer with Apple. Inc, Cupertino, CA, USA.

Christi K. Madsen (SM'03) received the Ph.D. degree in electrical engineering from Rutgers University, New Brunswick, NJ, USA, in 1996. She is currently a Professor of electrical and computer engineering with Texas A&M University, College Station, TX, USA. She is a Fellow of the Optical Society of America, a Distinguished Technical Staff Member with Bell Laboratories, Murray Hill, NJ, USA, and a Distinguished Lecturer for the IEEE Lasers and Electro-Optics Society.

Samuel Palermo (S'98–M'07–SM'17) received the B.S. and M.S. degrees in electrical engineering from Texas A&M University, College Station, TX, USA in 1997 and 1999, respectively, and the Ph.D. degree in electrical engineering from Stanford University, Stanford, CA, USA in 2007.

From 1999 to 2000, he was with Texas Instruments, Dallas, TX, USA, where he worked on the design of mixed-signal integrated circuits for high-speed serial data communication. From 2006 to 2008, he was with Intel Corporation, Hillsboro, OR, USA, where he worked on high-speed optical and electrical I/O architectures. In 2009, he joined the Department of Electrical and Computer Engineering, Texas A&M University, where he is currently an Associate Professor. His research interests include high-speed electrical and optical interconnect architectures, RF photonics, high performance clocking circuits, and integrated sensor systems.

Dr. Palermo is a recipient of a 2013 NSF-CAREER award. He is a member of Eta Kappa Nu. He is currently an Associate Editor for the IEEE SOLID-STATE CIRCUITS LETTERS and was previously an Associate Editor for the IEEE TRANSACTIONS ON CIRCUITS AND SYSTEM–II. He was also previously a Distinguished Lecturer for the IEEE Solid-State Circuits Society and on the IEEE CASS Board of Governors. He was a coauthor of the Jack Raper Award for Outstanding Technology-Directions Paper at the 2009 International Solid-State Circuits Conference, the Best Student Paper at the 2014 Midwest Symposium on Circuits and Systems, and the Best Student Paper at the 2016 Dallas Circuits and Systems Conference. He was the recipient of the Texas A&M University Department of Electrical and Computer Engineering Outstanding Professor Award in 2014 and the Engineering Faculty Fellow Award in 2015.

Kamran Entesari (M'06–SM'16) received the B.S. degree in electrical engineering from the Sharif University of Technology, Tehran, Iran, in 1995, the M.S. degree in electrical engineering from Tehran Polytechnic University, Tehran, in 1999, and the Ph.D. degree from the University of Michigan, Ann Arbor, MI, USA, in 2005. In 2006, he joined the Department of Electrical and Computer Engineering, Texas A&M University, College Station, TX, USA, where he is currently a Professor. His research interests include integrated RF photonics, RF/microwave/millimeter-wave integrated circuits and systems, microwave sensing, and reconfigurable RF/microwave antennas and filters.

Dr. Entesari is a Technical Program Committee Member of the IEEE RFIC Symposium. He was a recipient of 2018 and 2017 Qualcomm Faculty Award and 2011 National Science Foundation CAREER Award. He was a co-recipient of the 2009 Semiconductor Research Corporation Design Contest Second Project Award, the Best Student Paper Award of the IEEE RFIC Symposium in 2014 (second place), the IEEE Microwave Theory and Techniques Society in 2011 (third place), and the IEEE AP-S in 2013 (Honorable Mention). He is an Associate Editor for the IEEE MICROWAVE WIRELESS COMPONENTS LETTERS and a member of the editorial board for IEEE SOLID-STATE CIRCUITS LETTERS.